Automated Robotic Deburring Utilizing Active Force-controlled End-effector

Han-Hao Tsai, *Member, IEEE,* Yu-Chih Lin, and Jen-Yuan (James) Chang, *Senior Member, IEEE*

***Abstract*—This paper introduces an innovative automated robotic deburring approach, harnessing the capabilities of an active force-controlled end-effector in conjunction with a change-point algorithm. Human-led deburring process remains an indispensable operation even though it demands substantial time and cost. This significance is especially pronounced within the domain of aviation parts, where the presence of burrs can exert a profound influence on overall aerodynamic performance. Consequently, integration of robotic deburring has emerged as a viable substitute for labor-intensive manual procedures. Nevertheless, the inherent lack of stiffness in robotic arms often leads to challenges such as overcutting and unwanted vibrations, subsequently adversely affecting the surface finish of workpieces. To address these formidable problems, a one-degree-of-freedom active end-effector has been meticulously engineered, enabling the precise resolution of force-induced vibrations and overcutting problems through targeted force control in the normal direction. Furthermore, the issue of chattering has been effectively mitigated through the seamless incorporation of changepoint algorithm in the tangential direction. The proposed deburring algorithm has been verified through calibrated experiments, with results showing that surface profile variations for workpieces are four times smaller, underscoring its superior performance compared to the traditional position control method. Moreover, high-frequency force vibrations are effectively constrained within a range of ±1 N with the proposed method, and the moving average confirms the controller's ability to maintain stability and robustness, ensuring a consistent force control outcome.**

***Index Terms*—Automated Robotic Deburring, Active Force-controlled End-effector, Changepoint Algorithm.**

I. Introduction

Conventional burr removal is commonly performed concurrently with chamfering process. As depicted in Fig. 1, comprehensive deburring procedure can be bifurcated into two axes of motion: one aligned with the feed direction (i.e., the tangential direction), and the other orthogonal to it. According to [1], aircraft engine parts exhibit burr heights (normal direction) ranging from 0 to 1.5 mm, and thicknesses (tangential direction) between 0 to 0.23 mm. This data provides insights into the extent of burr projection and its repercussions on the material removal rate (MRR) in both the tangential and normal directions, respectively. Since the burr size can exhibit random variations within the specified range, this results in a significant fluctuation in cutting force during the deburring process when position control is employed [2]. Consequently, this leads to generation of severe chattering effects due to inherent lack of stiffness in robotic arms [3].

Given that the chamfer depth, denoted as the depth of cut (DOC), is directly correlated with the normal force exerted by the cutting tool [4], the imperative need arises for a precise force-controlled algorithm. This is essential to maintain a stable and reliable contact condition. Diverse force-controlled end-effectors have been harnessed to resolve this issue, employing a spectrum of control strategies. These strategies encompass stiffness control, impedance control [5], PID control [6-8], position/force hybrid control [8], and adaptive control schemes [10], etc. It is worth noting that the incorporation of force sensors into the aforementioned control structures may introduce non-collocated modes [11], potentially leading to unstable responses. Furthermore, conventional force/torque sensors exhibit limited bandwidth, which further compounds these challenges [12].

Due to the interplay between cutting forces in both the normal and tangential directions, adoption of a steadfast velocity control strategy for the robotic arm becomes essential to guarantee the preservation of a uniform feed rate per tooth of the cutting tool [13, 14]. Nevertheless, it is important to acknowledge that if the robotic arm lacks of sufficient stiffness, deflection between the workpiece and the robotic arm may ensue, eventually giving rise to undesirable chattering effects and stability issues [15, 16].
To address the aforementioned challenges, this paper introduces an active force-controlled end-effector designed to alleviate variations in chamfer depth resulting from force-induced vibrations in the normal direction. To circumvent potential adverse effects arising from the integration of force/torque sensors, we adopt a dual-observer-based control framework to ensure robust high-bandwidth control outcomes. Additionally, a changepoint algorithm is implemented in the tangential direction to detect the presence of large burrs [17], enabling the

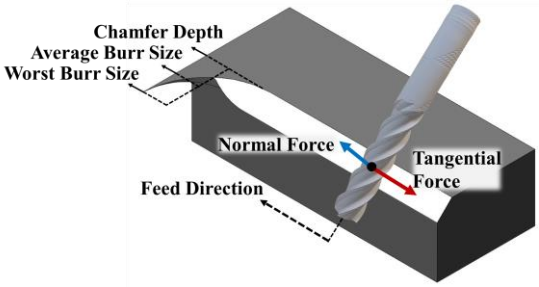

Fig.1. Schematic diagram of deburring process.

Manuscript received 08 December 2023; accepted 11 January 2024; date of publication 18 January 2024. This work was supported in part by the National Science and Technology Council (NSTC) of Taiwan with grant number 112-2218-E-007-017-.

H.-H. Tsai is with the Department of Power Mechanical Engineering, National Tsing Hua University, Hsinchu 30013, Taiwan (e-mail: pme0918087420@gapp.nthu.edu.tw).

Y.-C. Lin is with the Department of Power Mechanical Engineering, National Tsing Hua University, Hsinchu 30013, Taiwan (e-mail: jimmy1012zz@gapp.nthu.edu.tw).

J.-Y. Chang is with the Department of Power Mechanical Engineering, National Tsing Hua University, Hsinchu 30013, Taiwan, and also with the Department of Mechanical and Computer-Aided Engineering, National Formosa University, Huwei 63201, Taiwan. (e-mail: jychang@pme.nthu.edu.tw; james.chang@nfu.edu.tw).

adjustment of the robotic arm's feed rate to mitigate undesired deflection.

II. Design of the Active End-effector

Force-controlled deburring processes can be classified into two primary categories, namely through-the-arm control and around-the-arm control [6], respectively. Given that conventional robotic arms typically operate with control bandwidths below 500 Hz, adoption of an active end-effector (i.e., an around-the-arm control scheme) on the other hand can offers enhanced versatility and superior control outcomes. This rationale underpins the development of an active end-effector in this research.

As depicted in Fig. 2, the primary actuation component selected to meet the demanding force control requirements is the PBA CVC90 voice coil motor, known for its rapid response capabilities. To support the weight of the moving part of the structure, a set of parallel linear slides is positioned between the actuation unit and the cutting spindle system. Notably, an optical encoder is integrated within the active end-effector to obviate the need for the use of force/torque sensors. This decision serves the dual purpose of reducing the overall weight of the active end-effector and enabling efficient estimation of external disturbances and reaction forces by the controllers through Renishaw ATOM4T0-300 optical encoder system.

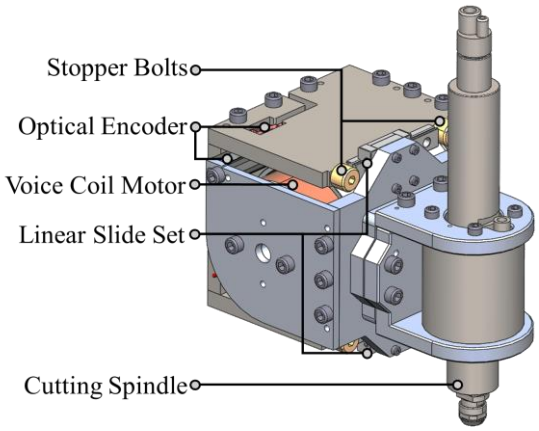

Fig. 2. Schematic drawing showing design of the active end-effector.

III. Dual-observer-based Control Framework

A. Basic Concept of the Controller

The controller consists of two fundamental components, as illustrated in Fig. 3, namely the disturbance observer (DOB) and the reaction force observer (RFOB), respectively. Implementation of the DOB serves to bolster the system's robustness against external disturbances by providing positive feedback of the observed disturbance signals [18-21]. Concurrently, the RFOB assumes the pivotal role of serving as the primary force feedback source, surpassing the conventional performance of force/torque sensors once the nominal parameters are well designed [22]. In crafting this dual-observer-based control system, it is imperative to develop a profound comprehension of how the adjustment of each specific parameter influences the system's performance. The transfer functions of the control system, as depicted in Fig. 3, can be articulated as

$$\begin{aligned}\hat{F}_{ext} = {} & C_f G_{env} F_{des} \\ & - \frac{\hat{M}_n \omega_R (s+\beta\omega_D)(s^2+M^{-1}D_{env}s+M^{-1}K_{env})}{(s+\omega_R)(s^2+(M^{-1}D_{env}+\alpha\omega_D)s+M^{-1}K_{env})}\eta - \frac{\omega_R}{s+\omega_R}\hat{F}_f \\ & + \frac{\hat{M}_n M^{-1}\omega_R (s+\beta\omega_D)s}{(s+\omega_R)(s^2+(M^{-1}D_{env}+\alpha\omega_D)s+M^{-1}K_{env})}F_{dis} \end{aligned} \quad (1)$$

, where the definitions of parameters are listed in Table 1, $\alpha = M_n K_f / M K_{fn}$, $\beta = M_n \hat{K}_{fn} / \hat{M}_n K_{fn}$, K_{env} stands for the stiffness of the contact environment, D_{env} is the damping of the contact environment, and

$$G_{env} = \frac{\hat{M}_n \omega_R (s+\omega_D)((\beta-\alpha)s^2+M^{-1}\beta D_{env}s+M^{-1}\beta K_{env})}{s(s+\omega_R)(s^2+(M^{-1}D_{env}+\alpha\omega_D)s+M^{-1}K_{env})} \quad (2)$$

is the open-loop transfer function of the DOB-based robust force control system. Based on the derivation outlined above, one can deduce that when the end-effector comes into contact with a rigid environment, the imaginary component of the poles in the transfer function from F_{des} to $\hat{F}_{ext}$ rises, leading to oscillatory behavior. Consequently, to suppress this oscillation behavior, it becomes necessary to increase the values of α and ω_D. However,

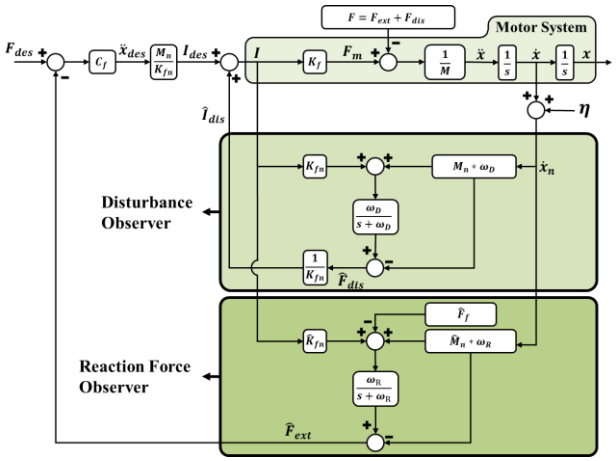

Fig. 3. Dual-observer-based control framework.

TABLE I
Parameter Definition of the Control Framework

Parameter	Definition
K_f	actual force constant of motor (N/A)
K_{fn}	nominal force constant in DOB (N/A)
$\hat{K}_{fn}$	nominal force constant in RFOB (N/A)
M	actual mass of motor system (kg)
M_n	nominal mass in DOB (kg)
$\hat{M}_n$	nominal mass in RFOB (kg)
ω_D	bandwidth of LPF in DOB (rad/s)
ω_R	bandwidth of LPF in RFOB (rad/s)
F_{dis}	external disturbance force (N)
$\hat{F}_{dis}$	estimated disturbance force (N)
F_{ext}	external force (N)
$\hat{F}_{ext}$	estimated external force (N)
F_{des}	desired force Input (N)
η	feedback noise (m/s)
$\hat{F}_f$	model-based estimations of disturbance terms (N)
C_f	outer-loop P-controller gain
s	complex number of Laplace transform
$x, \dot{x}, \ddot{x}$	position (m), velocity (m/s), and acceleration (m/s^2) of the motor

it's important to note that as α and ω_D are elevated, the system may encounter a waterbed effect [23], impacting the sensitivity functions of the system and potentially diminishing its overall resilience against feedback noise and external disturbances. Hence, there arises a need for a judicious trade-off when establishing the nominal parameters. Furthermore, the presence of the $(s+\omega_D)/(s+\omega_R)$ term in (2) underscores that adhering to the design constraint of $\omega_R > \omega_D$ can enhance the system's stability through the phase-lead effect.

B. Controller Design Simulations

To streamline the design procedure, we conducted a comprehensive analysis based on simulations and experiments to further explore the variations in nominal parameters and their impact on the system's control outcomes. Before delving into the design of nominal parameters, including M_n, K_{fn}, $\hat{M}_n$, $\hat{K}_{fn}$, it is essential to assign bandwidths of the low-pass filters in DOB and RFOB. In accordance with the design constraint and guided by prior research findings [24], ω_D is designated at 50 rad/s to forestall any stability decline. The selection of ω_R is predicated on the feedback bandwidth prerequisites, and it is established at 6283 rad/s, equivalent to 1000 Hz, in this research.

The measured mass of the moving part of the active end-effector is 4.087 kg, with a force constant of 40.63 N/A at the middle stroke. In pursuit of determining the tuning rules for the nominal parameters, a simplified deburring force model as provided by [6] is employed to simulate the system's responses, which can be expressed as

$$F_{ext} = K_f a^n f^m \tag{3}$$

, where K_f is the cutting stiffness, a stands for the DOF, f is the feed rate, n is the DOF exponent, and m is the feed-rate exponent. Here, the material is chosen to be stainless steel (SUS 304), and the P-controller gain of $C_f = 0.025$ is adopted. Additionally, feedback white noise is introduced into the system to observe variations in its robustness.

Fig. 4 illustrates how the tuning of M_n and K_{fn} influences system behavior, while Fig. 5 hones in on the effects of tuning $\hat{M}_n$ and $\hat{K}_{fn}$. The term "inner-loop step responses" pertains to the responses of the DOB, which predominantly dictate the steady-state values of the control system. Based on the simulation results, it becomes evident that by concurrently increasing the values of α and β, either by increasing M_n or decreasing K_{fn}, a shorter settling time can be achieved. However, it's important to note that this approach may come at the cost of potentially degrading system robustness. This is attributed to the heightened sensitivity peak resulting from the waterbed effect [22].

The derivation in (1) has elucidated that the sensitivity of the estimated force to external disturbances and feedback noise is contingent on the value of $\hat{M}_n$. This observation is further corroborated by the findings in Fig. 5(a). As $\hat{M}_n$ is increased, the impact of feedback noise becomes notably more pronounced. Moreover, the ratio of α to β, which is also influenced by the value of $\hat{M}_n$, can potentially lead to stability issues. If α surpasses β, one of the system's zeros is situated in the right-half plane, resulting in an undershoot as seen when

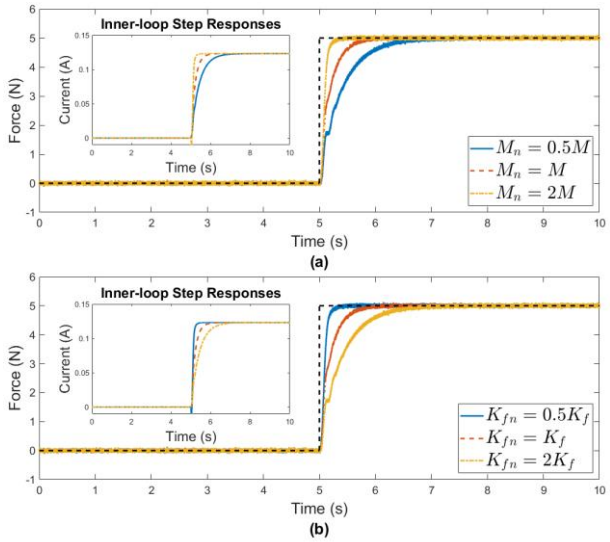

Fig. 4. Simulated system step response with different (a) M_n and (b) K_{fn} values.

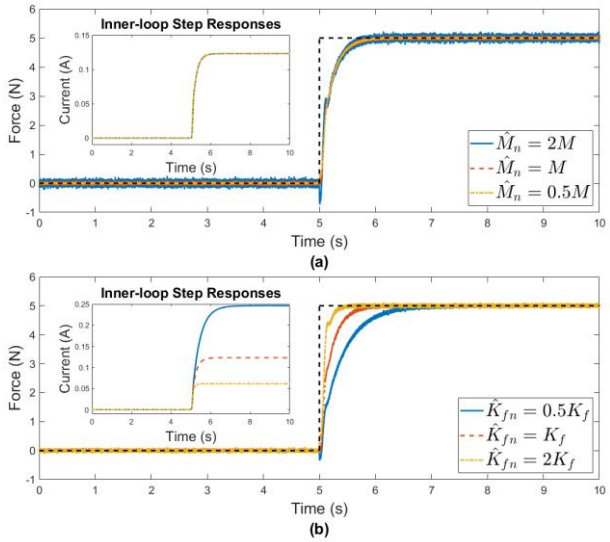

Fig. 5. Simulated system step response with different (a) $\hat{M}_n$ and (b) $\hat{K}_{fn}$ values.

$\hat{M}_n = 2M$ in Fig. 5(a). Hence, to avert the occurrence of a nonminimum phase zero, it is advisable to adhere to the design constraint of $\alpha < \beta$. While it's feasible to meet this design constraint by adjusting either $\hat{M}_n$ or $\hat{K}_{fn}$, as demonstrated by the simulation results, if the value of $\hat{K}_{fn}$ deviates from K_f, the inner-loop steady-state value will fail to converge to the desired force control value. This implies that the RFOB may no longer accurately estimate the external force. Therefore, it is imperative to set $\hat{K}_{fn}$ to the same value as the actual force constant to ensure precise force estimation results.

C. Reation Force Estimation Accuracy Validation

The implementation of the control framework on the active end-effector is facilitated through the selection of a BECKHOFF C6030 industrial computer to serve as the host for the real-time control system. Subsequently, the controller is discretized using the bilinear transformation method, and the sampling frequency is set at twice the control bandwidth

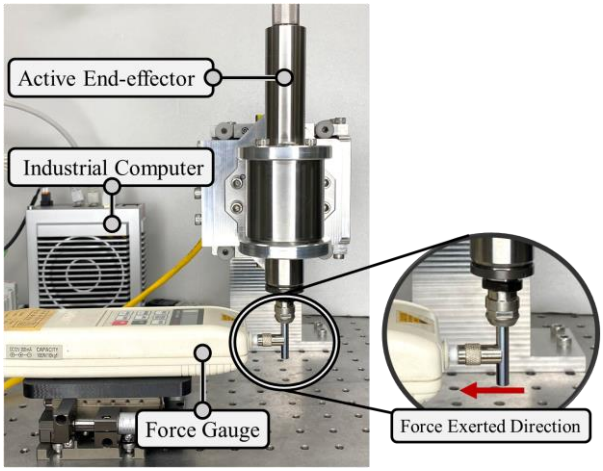

Fig. 6. Validation apparatus for of RFOB estimation.

TABLE II
NOMINAL PARAMETER VALUES

Parameter	Designed Value
K_{fn}	39.00 (N/A)
$\hat{K}_{fn}$	40.63 (N/A)
M_n	5.00 (kg)
$\hat{M}_n$	0.05 (kg)
ω_D	50 (rad/s)
ω_R	6283 (rad/s)
C_f	0.1

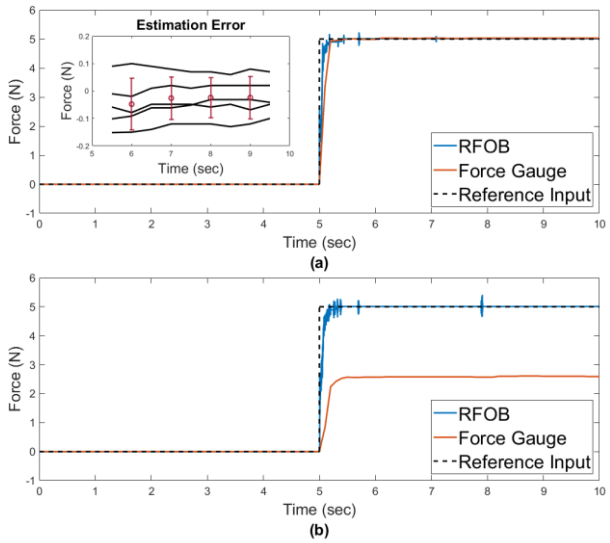

Fig. 7. Measured step responses for RFOB validation with (a) $\hat{K}_{fn} = K_f$ and (b) $\hat{K}_{fn} \neq K_f$.

requirement to ensure the prevention of signal aliasing. The voice coil motor receives a current command, while motion information, encompassing position and velocity data, is collected for software-related functionalities (e.g., safety limitations) and external force estimation via the RFOB.

Fig. 6 presents the experimental apparatus for validating the RFOB design, where an ALGOL HF-10 force gauge is employed to measure the actual force responses. The choice of nominal parameters is based on the design constraints mentioned earlier and a period of trial-and-error to finely adjust the transient response behavior, with the specific parameter values provided in Table 2.

Based on the experimental results showcased in Fig. 7, it is evident that the RFOB is indeed capable of offering precise estimations of external forces, yielding an absolute mean-square estimation error of approximately 0.064 N. Furthermore, with the incorporation of the controller, this active force-controlled end-effector attains a notable control bandwidth of approximately 1000 Hz, significantly surpassing conventional force/torque-sensor-based end-effectors [25].

IV. CHANGEPOINT ALGORITHM

To tailor the feed rate in response to variations in burr size along the cutting direction during machining operations, it is particularly crucial to devise an algorithm that can accurately identify the locations of burr size variation. This study collects real-time data on cutting forces through a force sensor and employs an algorithm to pinpoint areas with significant force variation. In the context of this paper, the locations of dramatic cutting force variation correspond to changes in burr size, and we define these locations as change points. To achieve this goal, we have implemented changepoint detection technology to analyze force information. The methods are categorized into offline and real-time based on their data processing approaches. Offline methods process all data at once for retrospective analysis, while real-time methods conduct analysis concurrently with data acquisition [26].

Considering the need to adjust feed rates in real-time based on immediate changes in burr size during the cutting process, real-time changepoint detection becomes a critical element. However, it must be acknowledged that complete real-time detection is impractical in practice due to the need to accumulate a sufficient number of samples for state estimation. Moreover, the chosen detection method must be both straightforward and rapid to minimize computational delays. In light of these considerations, the Bayesian Online Changepoint Detection (BOCPD) algorithm has been implemented [17].

The method is fundamentally rooted in Bayesian inference and facilitates the estimation of unknown parameters by continuously updating the probability distribution of observed data and prior information. It employs a probabilistic approach to estimate change points. To further streamline computation, this study employs Bayesian inference based on the Gaussian distribution model [27], establishing a pivotal link between the posterior distribution and observational data through the following relationship as

$$P(X_{new}|X_{1:t}) = \int P(X_{new}|\alpha)\, P(\alpha|X_{1:t}), \tag{4}$$

and define model parameter as

$$\alpha_k = \begin{cases} 0 & \text{changepoint occur} \\ \alpha_{k-1} + 1 & \text{otherwise} \end{cases}. \tag{5}$$

The concluding step involves presenting the mathematical equation in a discrete and recursive format

$$P(\alpha_k \cap X_{1:k}) = \sum_{r_{k-1}} P(\alpha_{k-1} \cap X_{1:k-1}) P(r_k|r_{k-1}) P\left(X_k \middle| r_k \cap {X_k}^{\beta}\right) \tag{6}$$

, where the term ${X_k}^{\beta}$ encompasses the observed data associated

with β_{th} time, which implies that when a changepoint occurs at time β, we exclusively focus on data from time β onwards. The online changepoint detection and overall robot arm control architecture is presented in the following algorithm as

Algorithm1: Bayesian Online Changepoint Detection

Input: The force data from force sensor
Output: The cutting feed rate
initialize model parameter, mean and variance
robot arm commences the cutting process.
while new data is available **do**:
  calculate changepoint probabilities
  if changepoint occur **then**
    if current_force>previous_force **then**
    decrease robotic arm feed rate
    else
    increase robotic arm feed rate
  else
  maintain robotic arm feed rate
  end if
  update the statistical probability
end while

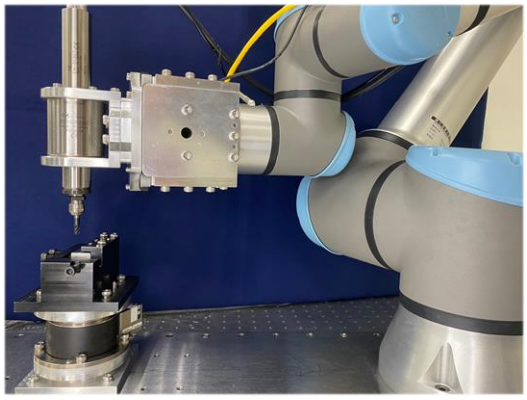

Fig. 8. Experimental setup for robotic deburring with the proposed force-control method.

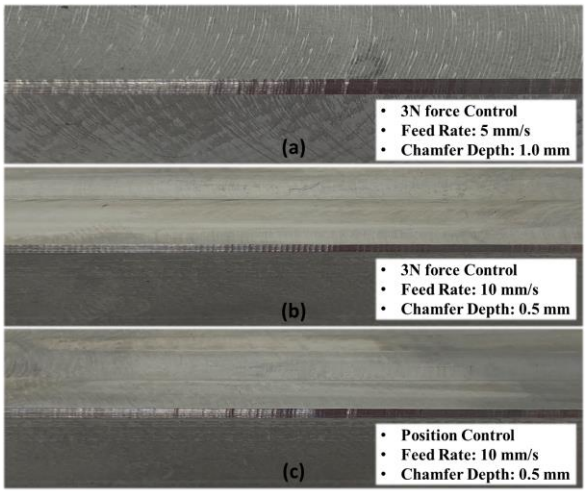

Fig. 9. Deburring experimental results (size of workpieces: 50 × 20 × 13.5 mm) utilizing force control with (a) 5 mm/s and (b) 10 mm/s feed rate, and position control with 10 mm/s feed rate in (c).

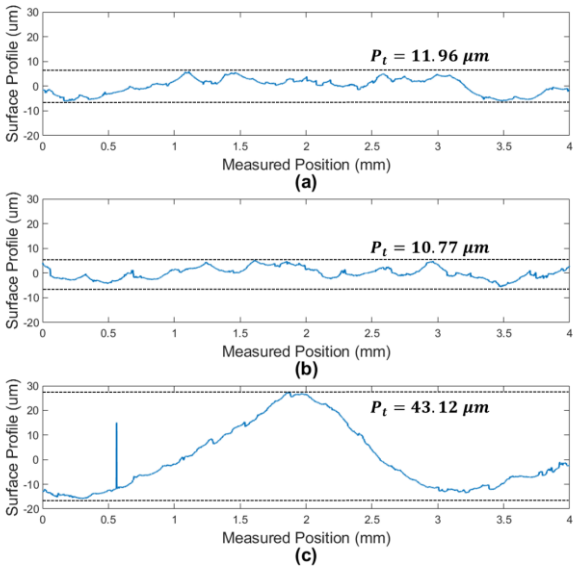

Fig. 10. Surface profile resulted from force control with (a) 5 mm/s and (b) 10 mm/s feed rate, and (c) from position control with 10 mm/s feed rate.

V. EXPERIMENTS

For the robot deburring operations, a UR10e collaborative robot is outfitted with the active end-effector. The dual-observer-based control framework is applied along the normal direction to regulate the chamfer depth variations. Simultaneously, the changepoint algorithm is deployed in the tangential direction to adjust the feed rate of the robotic arm, thereby ensuring the stabilization of the MRR throughout the overall deburring process. The comprehensive experimental setup is depicted in Fig. 8, featuring the attachment of an ATI force/torque sensor to the fixture. This sensor is employed to detect the actual force responses, enabling the changepoint algorithm to dynamically adjust the feed rate of the robot based on the acquired data.

Fig. 9 and Fig.10 present the deburring results under the condition where the tangential projected area remains constant, indicating that the feed rate can be maintained at a consistent value throughout the entire deburring process. As depicted in the results, an increase in the feed rate from 5 mm/s to 10 mm/s results in a shallower chamfer depth, underscoring the significant impact of the feed rate on the overall deburring process. Furthermore, the force control results highlight that even though the chamfer depth is twice that achieved under position control conditions, there is a noteworthy enhancement in the total height of the profile of the workpiece denoted as P_t in Fig. 10, which is the vertical distance between the maximum profile peak height and the maximum profile valley depth along the evaluation length. Additionally, the surface roughness, R_t, the total height of the roughness profile, also demonstrates improvement, decreasing from 27.977 to 6.816 μm under the 10 mm/s feed rate.

As illustrated in Fig. 11, the deburring controller and algorithm are applied to further test the feasibility of the proposed method by introducing a 0.5 mm chamfer depth

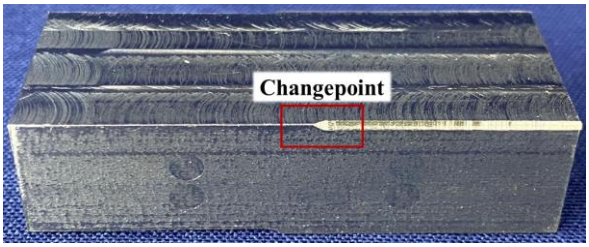

Fig. 11. Workpiece showing chamfer depth difference distinguished by the highlighted changepoint.

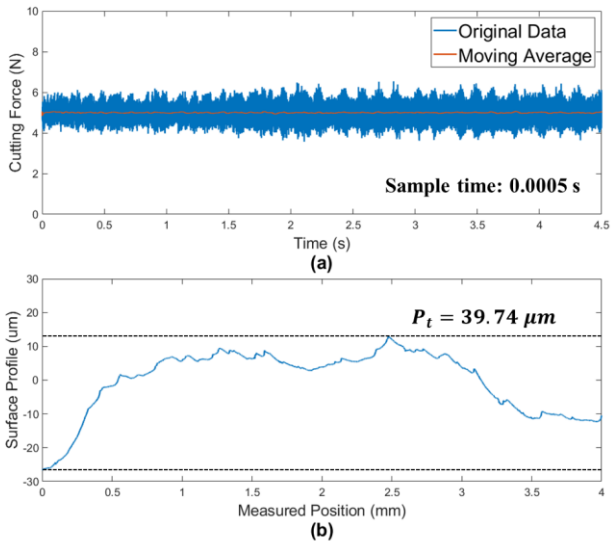

Fig. 12. Experimental data showing (a) cutting force when encountering chamfer depth difference and (b) the surface profile around changepoint.

difference at the midpoint of the workpiece. To achieve a smooth chamfer surface, a force control of 5 N is implemented, and the experimental results are depicted in Fig. 12. As indicated in Fig. 12(a), the high-frequency force vibrations are effectively confined within a range of ±1 N, and the moving average further demonstrates that the controller maintains its stability and robustness, resulting in a consistent force control outcome. Furthermore, upon closer examination of the surface roughness results in the vicinity of the changepoint outlined in Fig. 11, a total profile height, P_t, of 39.74 μm and a surface roughness, R_a, of 6.44 μm are achieved after the deburring process, even in the presence of an initial 0.5 mm chamfer depth difference.

VI. Conclusion

This paper introduces an innovative automated robotic deburring approach that combines an active force-controlled end-effector in the normal direction with a changepoint algorithm in the tangential direction of the model workpiece during deburring process. Through calibrated experiments, the active force-controlled end-effector has been demonstrated to be able to achieve high-precision force control results with the utilization of a dual-observer based control framework. Additionally, the experimental validation of the changepoint algorithm showcases its effectiveness in assisting the force controller to maintain a stable material removal rate (MRR) by adjusting the feed rate of the robotic arm. The algorithm is implemented on a UR10e robot, and a series of deburring experiments have been conducted, confirming the efficacy of the force control algorithm by delivering improved surface roughness results compared to conventional position-controlled deburring algorithms.

References

[1] M. G. Her and H. Kazerooni, "Automated robotic deburring of parts using compliance control," *Journal of Dynamic Systems, Measurement, and Control*, vol. 113, no. 1, pp. 60-66, 1991.

[2] J. C. Aurich, D. Dornfeld, P. J. Arrazola, V. Franke, L. Leitz, and S. Min, "Burrs—Analysis, control and removal," *CIRP Annals*, vol. 58, no. 2, pp. 519-542, 2009/01/01/ 2009.

[3] Tony L. Schmitz, K. Scott Smith, "Machining Dynamics-Frequency Response to Improved Productivity," *Springer International Publishing AG, Springer Nature 2019*, 2nd ed., 2018.

[4] G. Miller, R. A. Irani, and M. Ahmadi, "Application of mechanistic force models to features of arbitrary geometry at low material removal rate," *The International Journal of Advanced Manufacturing Technology*, vol. 117, no. 9, pp. 2741-2754, 2021.

[5] J. Seul, T. C. Hsia, and R. G. Bonitz, "Force tracking impedance control of robot manipulators under unknown environment," *IEEE Transactions on Control Systems Technology*, vol. 12, no. 3, pp. 474-483, 2004.

[6] G. M. Bone and M. A. Elbestawi, "Robotic force control for deburring using an active end effector," *Robotics and Computer-Integrated Manufacturing, Robotica*, vol. 7, no. 4, pp. 303-308, 1989.

[7] G. M. Bone and M. A. Elbestawi, "Force control for robotic deburring," *Robotics and Computer-Integrated Manufacturing*, vol. 8, no. 2, pp. 87-96, 1991.

[8] F. Chen, H. Zhao, D. Li, L. Chen, C. Tan, and H. Ding, "Contact force control and vibration suppression in robotic polishing with a smart end effector," *Robotics and Computer-Integrated Manufacturing*, vol. 57, pp. 391-403, 2019.

[9] Z. Ma, A.-N. Poo, M. H. Ang, G.-S. Hong, and H.-H. See, "Design and control of an end-effector for industrial finishing applications," *Robotics and Computer-Integrated Manufacturing*, vol. 53, pp. 240-253, 2018.

[10] S. Lakshminarayanan, S. Kana, D. M. Mohan, O. M. Manyar, D. Then, and D. Campolo, "An adaptive framework for robotic polishing based on impedance control," *The International Journal of Advanced Manufacturing Technology*, vol. 112, no. 1, pp. 401-417, 2021.

[11] S. D. Eppinger and W. P. Seering, "Three dynamic problems in robot force control," *International Conference on Robotics and Automation*, pp. 392-397, vol.1, 1989.

[12] S. Katsura, Y. Matsumoto, and K. Ohnishi, "Analysis and experimental validation of force bandwidth for force control," *IEEE Transactions on Industrial Electronics*, vol. 53, no. 3, pp. 922-928, 2006.

[13] A. Burghardt, D. Szybicki, K. Kurc, and M. Muszyńska, "Experimental study of Inconel 718 surface treatment by edge robotic deburring with force control," *International Journal of Applied Mechanics and Engineering*, vol. 21, pp. 987-995, 12/01 2016.

[14] G. Miller, R. A. Irani, and M. Ahmadi, "The application of mechanistic cutting force models for robotic deburring," *The International Journal of Advanced Manufacturing Technology*, vol. 115, no. 1, pp. 199-212, 2021.

[15] P. Zengxi and Z. Hui, "Analysis and suppression of chatter in robotic machining process," in 2007 International Conference on Control, Automation and Systems, 17-20 Oct. 2007, pp. 595-600.

[16] S. Eppinger and W. Seering, "Introduction to dynamic models for robot force control," IEEE Control Systems Magazine, vol. 7, no. 2, pp. 48-52, 1987.

[17] R. P. Adams and D. J. MacKay, "Bayesian Online Changepoint Detection," *arXiv preprint arXiv:0710.3742*, 2007.

[18] K. Ohnishi, M. Shibata, and T. Murakami, "Motion control for advanced mechatronics," IEEE/ASME Transactions on Mechatronics, vol. 1, no. 1, pp. 56-67, 1996.

[19] E. Sariyildiz, R. Oboe, and K. Ohnishi, "Disturbance Observer-Based Robust Control and Its Applications: 35th Anniversary Overview," *IEEE Transactions on Industrial Electronics*, vol. 67, no. 3, pp. 2042-2053, 2020.

[20] S. Katsura, Y. Matsumoto, and K. Ohnishi, "Modeling of Force Sensing and Validation of Disturbance Observer for Force Control," *IEEE Transactions on Industrial Electronics*, vol. 54, no. 1, pp. 530-538, 2007.

[21] E. Sariyildiz, "A Note on the Robustness of the Disturbance Observer-Based Robust Control Systems," Journal of Dynamic Systems, Measurement, and Control, vol. 144, no. 9, 2022.
[22] E. Sariyildiz and K. Ohnishi, "An Acceleration-Based Robust Motion Controller Design for a Novel Series Elastic Actuator," *IEEE Transactions on Industrial Electronics*, vol. 62, no. 1, pp. 414-422, 2015.
[23] H. Kurumatani and S. Katsura, "Design of Nominal Parameters for Robust Sensorless Force Control Based on Disturbance Observer," *IEEJ Journal of Industry Applications*, vol. 8, no. 2, pp. 342-351, 2019.
[24] E. Sariyildiz and K. Ohnishi, "A Guide to Design Disturbance Observer," *Journal of Dynamic Systems, Measurement, and Control*, vol. 136, no. 2, 2013.
[25] J. Li *et al.*, "A High-Bandwidth End-Effector With Active Force Control for Robotic Polishing," *IEEE Access*, vol. 8, pp. 169122-169135, 2020.
[26] S. Aminikhanghahi and D. J. Cook, "A survey of methods for time series change point detection," Knowledge and information systems, vol. 51, no. 2, pp. 339-367, 2017.
[27] K. P. Murphy, "Conjugate Bayesian analysis of the Gaussian distribution," def, vol. 1, no. 2σ2, p. 16, 2007.

Han-Hao Tsai received *B.S.* and *M.S. degree* of mechanical engineering in 2020 and 2022 from *National Tsing Hua University, Taiwan*. He is currently a PhD student in Vibrations, Mechatronics and Robotics Laboratories, *Department of Power Mechanical Engineering, National Tsing Hua University, Taiwan*. He is a Student Member of IEEE, and a Member of IEEE Control Systems Society. His major fields of study include control theory, robotics, motion control, and mechatronics.

Yu-Chih Lin received *B.S. degree* in 2022 from *National Central University*. He is currently a master student in Vibrations, Mechatronics and Robotics Laboratories, *Department of Power Mechanical Engineering, National Tsing Hua University, Taiwan*. His major fields of research include robotics, robot machining, and robot force control.

Jen-Yuan Chang received *B.S. degree* in 1994 from *National Central University, Taiwan* and *M.S.* and *Ph.D. degrees* in 1998 and 2001, respectively from *Carnegie Mellon University, USA*, all in Mechanical Engineering. He is currently a Chair Professor of National Tsing Hua University and Chair Professor of *National Formosa University, Taiwan*. He was an ASEE/NRC Faculty Research Fellow at US AFRL on vibrations of integrated bladed rotors and was with IBM/HGST on R&D of high-end magnetic disk storage technologies. A former Division Chair of ASME-ISPS and Vice-Chair of ASME Strategic Planning Committee, Dr. Chang was the recipient of the ASME-ISPS Division's Distinguished Institution Award, Outstanding Contribution Award, and Ministry of Science and Technology's Outstanding Research Award. He is Fellow of ASME, CSME, RST, STAM, and Senior Member of IEEE.